HiSST: 3rd International Conference on
High-Speed Vehicle Science Technology

14–19 April 2024, Busan, Korea

Comparison of Models for Aerothermal Load Prediction using Coupled Trajectory Simulations of a High Lift Reentry Vehicle

Marius Franze[1], *Fynn Barz*[2]

Abstract

This paper uses a high lift reentry vehicle geometry to get unsteady RANS results for aerothermal heating on the out- and inside of the body using the DLR TAU code coupled with a structural solver. The DLR CoNF²aS² toolchain (Coupled Numerical Fluid Flight Mechanic And Structure Simulation) is used to perform a coupled Fluid/Structure/Flight-mechanic simulation along the given flight trajectory. From these high-fidelity results in a second step a database along the trajectory is produced, containing the heat flux and temperature distribution on the surface. Afterwards a modified trajectory is calculated and the heating gets interpolated from the database heat flux along the new trajectory and compared with the initial computed flight path. This will speed up the design process of future vehicle geometries regarding TPS and trajectory development.

Keywords: *High Lift Reentry Vehicle, CoNF2aS2, Coupled CFD-CSM Simulation, Aerothermal Loads*

Nomenclature

Abbreviations

BBE	Base Bottom Edge
CFD	Computational fluid dynamics
CoNF²aS²	Coupled Numerical Fluid Flight Mechanic And Structure Simulation
(AT)DB	(Aero-Thermal) Database
DLR	German Aerospace Center
FFTB	Flux Forward Temperature Back
FSI	Fluid-Structure-Interaction
HF	Heatflux
HLRV	High Lift Reentry Vehicle
TFFB	Temperature Forward Flux Back
TPS	Thermal Protection System
WR	Wave Rider

Latin

h	Altitude
M	Mach number
p	Pressure
$\dot{q}$	Heatflux
T	Temperature
t	Time

Greek

ρ	Density
λ	Thermal Conductivity Coefficient
Ω	Coupling Domain

Superscripts

f	Fluid
s	Structure

Subscripts

LE	Leading Edge
n	Number of timesteps
ref	Reference Values

1. Introduction

High Lift Reentry Vehicles (HLRV) are increasing in interest during the last years after their intensive studies in the 80s, 90s and 00s back when they have been known as waveriders. Huge designs like the famous Sänger as a space transport system gained attention as well as pure research vehicles like the successfully flown Boeing X-51 Waverider (WR) in 2013. They all are meant to fly in much higher

[1]*German Aerospace Center (DLR), Institute of Aerodynamics and Flow Technology, Spacecraft, Lilienthalplatz 7, 38108 Braunschweig, Germany, Marius.Franze@dlr.de*

[2]*German Aerospace Center (DLR), Institute of Aerodynamics and Flow Technology, Spacecraft, Lilienthalplatz 7, 38108 Braunschweig, Germany, Fynn.Barz@dlr.de*

altitudes than conventional airplanes over a long duration in time with mach numbers often bigger than 7. Last but not least, this makes them of special interest from a defense stand point as Hypersonic Glide Vehicles (HGV).

To get a better understanding of the challenging flow conditions and heating effects especially, a high-fidelity fluid/structure/flight-mechanic coupled environment was used to calculate the flow and resulting internal heating of a generic high lift reentry vehicle using a generic trajectory. The interpolation between the solver was accomplished in the FlowSimulator Framework using the coupling environment CoNF2aS2 (Coupled Numerical Fluid Flight-mechanic And Structure Simulation), developed within the spacecraft department. FlowSimulator enables highly efficient parallel data management, interpolation and exchange between different solvers and has been developed towards the goal of virtual flight testing [12, 10], making it perfect for the integration basis of $CoNF^2aS^2$, where spacecraft specific implementations can be added on top.

From an unsteady numerical evaluation point of view, high lift reentry vehicles glide a long time during their flight path, which makes it rather intensive in terms of computational costs to be analyzed numerically, depending on the level of detail. On the other hand, wind tunnel experiments either lack of the duration, the necessary accuracy or both, especially for higher mach numbers, where real gas effects are evolving. Reentry flight experiments can be expensive as well, especially if they are intended to replicate real flight conditions at real sized geometries.

For the high fidelity reference purpose, these following calculations will be performed by a equilibrium and non-equilibrium gas model on the fluid side and temperature dependent non-linear material models at the structures side of the coupling process. As these models are very time consuming and computationally intensive, faster methods are evaluated inside this paper and validated against the high fidelity solutions. To speed up the coupled environment to the point of optimization capabilities during the design process, lower fidelity models for fluid and structural solving got implemented. As a second middle-fidelity method for the flow solver, an interpolation of predefined calculated heat fluxes obtained by few discrete high fidelity solutions in an engineering database along the trajectory is implemented as described by Laureti and Karl [7, 8]. The structural part can be complemented by simple heat conduction equations or ANSYS as the structural solver.

These models are much faster, but lack the accuracy of the high fidelity models. The comparison of these models along each other by means of the generic HLRV is the first goal and main result of this paper to get an overall idea of the error range for each of the used methods.

2. Generic Use Case

2.1. Analyzed Trajectories

Figure 1 presents altitude h, angle of attack α and the corresponding mach number M over time of the generic trajectory. The motor separation at $t = 0$ s is at an altitude of 85 km with a mach number of 12.3 for the initial reference trajectory. This maneuver is followed by a dipping reentry curve down to 24.4 km at $t = 132$ s and directly pitching up to 32.3 km. The cruise phase starts at $t = 200$ s at an altitude of around 30 km with a mach number between 10.5 to 10.0. The angle of attack is typically significant for a classic reentry, rising from the beginning to $\alpha = 12°$ and falling afterwards below 0° at the dipping point at the pitch up maneuver. At the beginning of the glide phase it oscillates between −2° and 1° slowly converging towards 0°.

The second shown trajectory in dashed lines has its starting altitude at 75 km and will be used as an off-design use case for the following analysis. It shares the same angle of attack and velocity, but has a matched mach number to the adapted altitude and its atmospheric conditions at each time point. The glide phase results in an mach number of 10.2 to 9.8 and approaches an altitude of 35 km. Both trajectories have not been calculated by means of fully coupled 6DoF-calculations, but are designed to be representative for the generic use case.

The points marked in the altitude plot are used for the later described database generation for the bilinear heatflux interpolation.

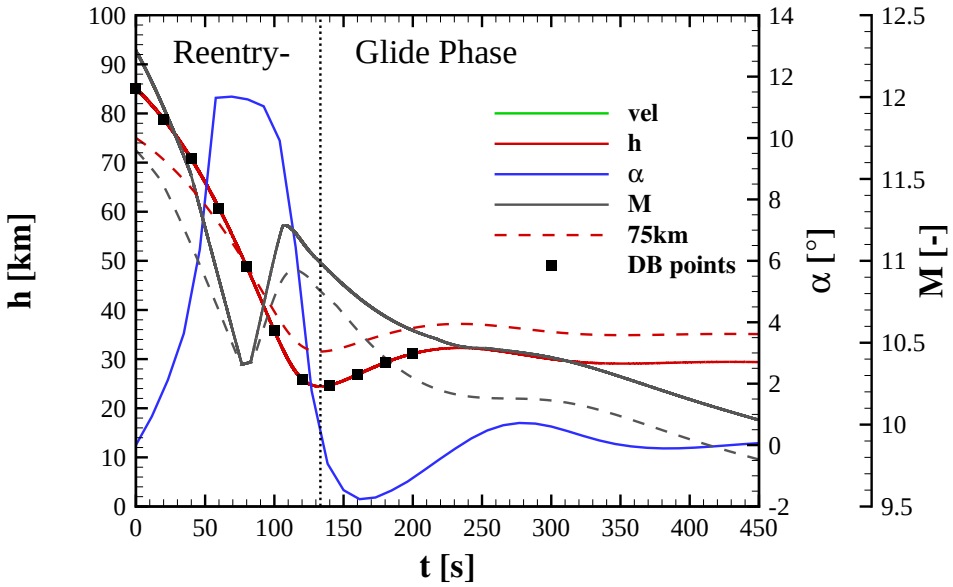

Fig 1. Generic trajectory including altitude, angle of attack and mach number for starting altitude at 85 km and 75 km with marked points for database generation.

2.2. Geometry of High Lift Reentry Vehicle

High Lift Reentry Vehicles (HLRV) usually have a rather high Lift to Drag ratio, especially if compared to classic sounding rockets. Depending on the geometry maximum values between 4 to 7 can be achieved if viscous effects have been considered during the design [3]. The HLRV illustrated in figure 2 reaches similar values, depending on the trajectory and its corresponding velocity.

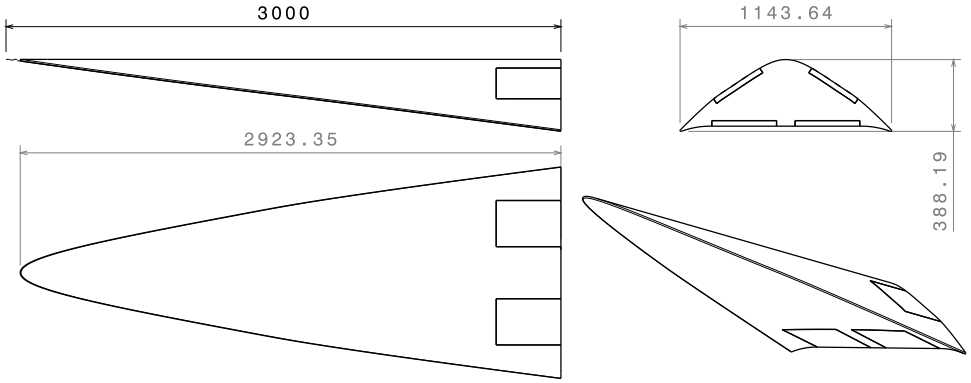

Fig 2. HLRV Geometry in different views and reference sizes in mm.

The reference length is $l_{ref} = 3000$ mm without the rounded leading edge. The leading edge radius is calculated from $r_{LE} = 0.0015 \cdot L_{ref} = 4.5$ mm and reduces the total length and width of the vehicle to obtain a tangential transition from the luv side to the leading edge to the lee side of the spacecraft. The length results in 2923 mm and the width in 1144 mm. The illustrated body flaps have not been modeled in the simulations to speed up the calculations as the main focus of this work is on the heating of the main body.

The body itself was designed with an osculating cone method at a design mach number of 10 with a semi-vertical angle of the conical shock between rotational axis and the shock itself of 10°, described in more detail by Barz [2].

3. Numerical Methods

This paper compares two different approaches of coupled solvers. The first, called high fidelity, is a fully coupled CFD solver DLR TAU as a loose scheme with the CSM solver Ansys. It is implemented withing the $CoNF^2aS^2$ process chain, which builds on top of the FlowSimulator [12]. The data exchange is realised withing the RAM of the computer to save IO time and written and read files, which can slow down this kind of computation, depending on the size of the problems.

The starting point of the unsteady FSI calculation is at t=0s at an altitude of 85 km where the laws of continuum flow are valid. At higher altitude the Knudsen number would be bigger than 0.01 at the boarder to rarefied gases where slip flow effects start to evolve at such low densities that the molecular mean free path is not negligible.

Independent of the flow solver the ICAO [11] atmosphere is used as atmospheric conditions and set at each calculated time step according to the flown altitude.

The flight itself is applied by a forced motion on the CFD mesh. The inflow condition is set to zero, but the mesh itself moves with the given trajectory parameters position, velocity, rotational rates and angles of attack. For this paper there is no flight mechanic solution involved although $CoNF^2aS^2$ is capable to do so.

3.1. Coupling of Solvers

The load transfer is achieved by marker based interpolations from the CFD interface mesh to the CSM interface mesh and vice versa. In this work the interface meshes consist of every surface points of the outer shells of each mesh because the highly parallel interpolation routines of FlowSimulator scales well. $CoNF^2aS^2$ is capable of a pure deformation and thermal analysis simulation in steady and unsteady cases as well as combined solutions where deformations and thermal heating gets calculated in one single run.

Therefore for the load transfer it captures forces and moment from the CFD solver to the CSM mesh, which on the other hand then gives displacements and rotations on each element back. Then the CFD mesh gets deformed as well and the next coupling step will be computed. For thermal analysis the CFD mesh either spends heatflux to the CSM solver and gets surface temperatures back ($FFTB$ - *Flux Forward Temperature Back*) or the resulting surface temperature from the CFD calculation gets interpolated on the CSM mesh, which gives the heatflux back ($TFFB$ - *Temperature Forward Flux Back*). Depending on the problem one or the other method is more numerically stable. In this work the FFTB scheme is used.

Figure 3 shows the loose coupling of the partitioned single domain solver for CFD and CSM. At the first coupling step an steady fluid solution is generated at $t = 0$ s. Then the initial conditions gets exchanged at 1.0 and the CSM solver calculates its heating. Then the newly generated surface temperature gets interpolated on the CFD mesh and a new heatflux gets calculated towards the new time step t_{n+1} resulting in the first predictor step. Depending on the amount of subcycles this looping procedure can be run through several times reaching an abort criteria, after which the next time step gets calculated. Depending on the altitude and density of the flight path the coupling procedure needs about 3 to 10 inner cycles to reach its abort criteria. If the heatflux gets bigger at denser atmospheres the process needs more inner cycles.

The middle fidelity approach using the database bilinear heatflux interpolation does not gain much accuracy using the inner cycles. There the inner cycles are set to 1, meaning just calculating the predictor steps.

3.2. High Fidelity Approach

The high fidelity solvers used in this paper are the DLR TAU code for the fluid domain and the commercially available suite *ANSYS Mechanical* in version 2022R2 [1] for the structure domain. The calculated time steps are $\Delta t = 0.1$ s.

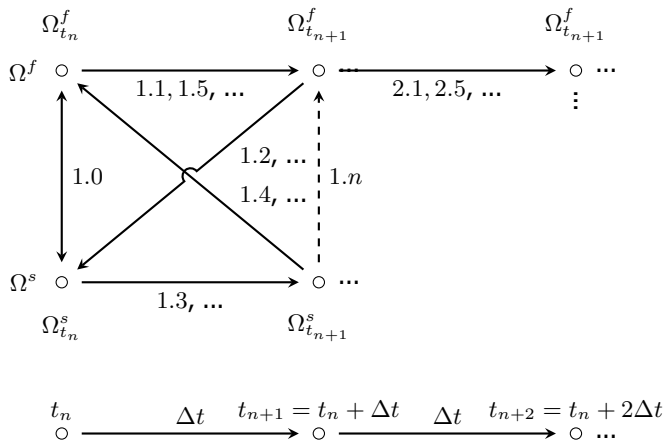

Fig 3. Loose partitioned Fluid-Structure-Interaction (FSI) coupling scheme of the single domain solver for fluid Ω^f and structure Ω^s.

3.2.1. DLR TAU code - Fluid domain

DLR TAU is a three-dimensional parallel hybrid multigrid code and has been validated for subsonic, transonic and hypersonic flows (shown in, e.g.: Schwamborn et al. [14], Langer et al. [6] or Mack et al. [9]). It solves the Reynolds-Averaged Navier-Stokes (RANS) equations using a second-order finite-volume method and is adapted for large scale simulations on high performance cluster (HPC) systems. The shown efficiency of the code makes it widely used in industrial as well as scientific applications for steady and unsteady flow phenomena and whole air- and spacecraft configurations. Under the variety of available turbulence models the Spalar-Allmaras one equation model in its negative formulation is used [15]. This model has already proven to be robust and sufficient for high speed vehicles [13].

An AUSMDV flux vector splitting upwind scheme [16] has been used, which can be used over the whole flight trajectory. To minimize possible uncertainties regarding laminar turbulent boundary layer transition the walls of the HLRV are modeled as fully turbulent.

As thermodynamic model within DLR TAU an equilibrium (EQ) as well as a non-equilibrium gas model (NEQ) is used, both in thermal equilibrium. The equilibrium model uses 11 gas species because it can be computed much faster where the non-equilibrium model only contains 5 species, because each add an energy equation to be solved during runtime as Gupta [5] presents, all shown in table 1. For the EQ model a gas mixture database can be generated a priori using Polynomials provided by Gordon [4], which saves computational time during the solution process. Each model set a mass fraction of 76 % N_2 an 24 % O_2 as inflow condition. The production of the residual species get calculated during the calculation according to local mixture rules depending on pressure, density and gas composition.

Table 1. Used thermodynamic gas models and calculated species.

Model	Number of Species	Species
EQ	11	N_2, O_2, NO, N, O, N_2^+, O_2^+, NO^+, N^+, O^+, e^-
NEQ	5	N_2, O_2, NO, N, O

The dimensionless value y^+ is well under 0.7 for the luv and lee surfaces of the HLRV along the whole trajectory just reaching 1.5 at the stagnation point at the nose tip in the worst case scenario during a short period of time around the dipping point at $t = 132$ s.

Figure 4 shows the hybrid mesh of the fluid domain. The field mesh contains 29.9 M nodes, whereas the surface alone consists of 0.72 M points. For this type of geometry the mesh is rather fine resolved, which is necessary to get a smooth temperature distribution on the surface. The leading edge has structured

quad elements, the remaining luv and lee sides as well as base plane of the vehicle have unstructured triangles to save points.

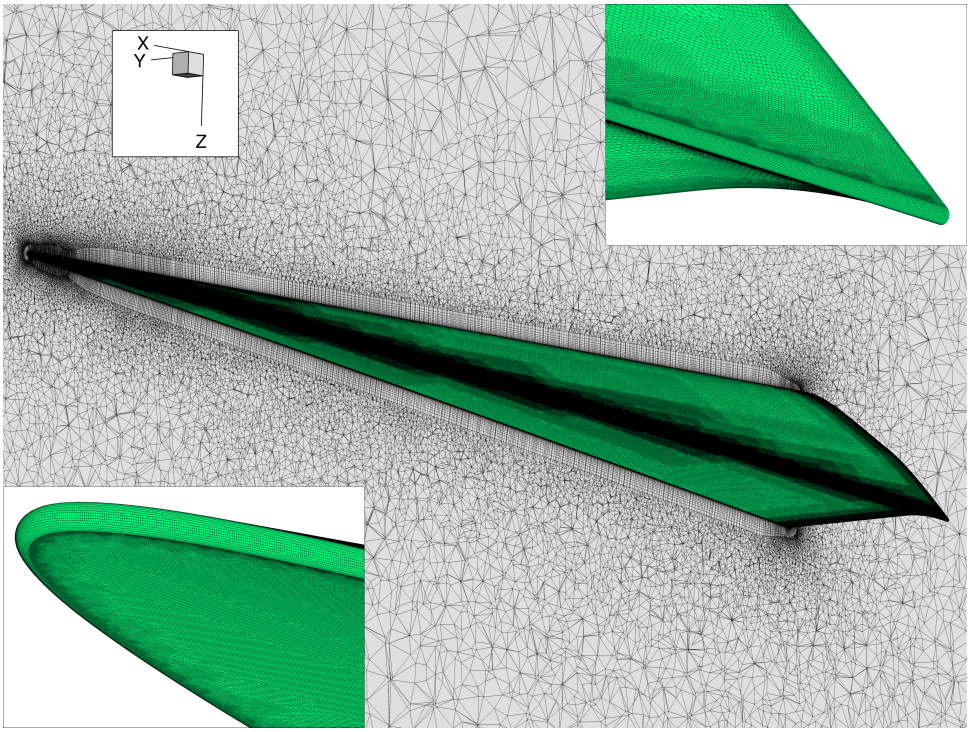

Fig 4. CFD surface mesh and $y = 0$ slice.

3.2.2. Ansys - Structure domain

As high fidelity structural solver the commercially available suite called *Ansys Mechanical 2022 R2* is applied by means of a 3D transient thermal analysis sparse solution. It gets the heatflux from the fluid domain, calculated the structural heating and gives the resulting surface temperatures back.

Figure 5(a) shows the surface mesh, which again, is rather fine resolved to get smooth transitions along the bodies. Within the CSM solver, quadratic tetrahedra elements are used for each of the parts, which are displayed in figure 5(b). The model consists of a single body with a three layer material mix, to save additional contact element points and speed up processing and solution time of each structure calculating loop.

The total number of grid points equal to 5.2 M nodes for the volume mesh alone and 0.15 M points for the surface.

The structure model consists of three layers listed in table 2. The outer layer is a high temperature resisting ceramic developed within the DLR. The isolation is a industrial available material called Zirkar ZO/ZYK which can be loaded continuously up to $T < 2200°$ and has a melting point of $T = 2590\,°$C and a temperature dependent thermal conductivity coefficient between $0.126\,\mathrm{W/(m\,K)} < \lambda < 0.661\,\mathrm{W/(m\,K)}$.

The inner hull body is modeled with a conventional aluminum layer, to keep the mass down and distribute the residual heat inside the body evenly. The boundary of the inner surface is perfectly insulated with a heatflux of zero, containing the total amount of heat inside the modeled bodies. Radiation is applied on the outer surface with an emissivity of 0.8, which can be achieved for C/C-SiC.

3.3. Mid Fidelity Approach

Usually depending on the reentry mission profile the TPS is a crucial point in design for these configurations. It needs to withstand the high heatfluxes while beeing robust and light-weight. It now is possible to calculate the flow conditions at each time point, like it is presented for the high fidelity approach, but

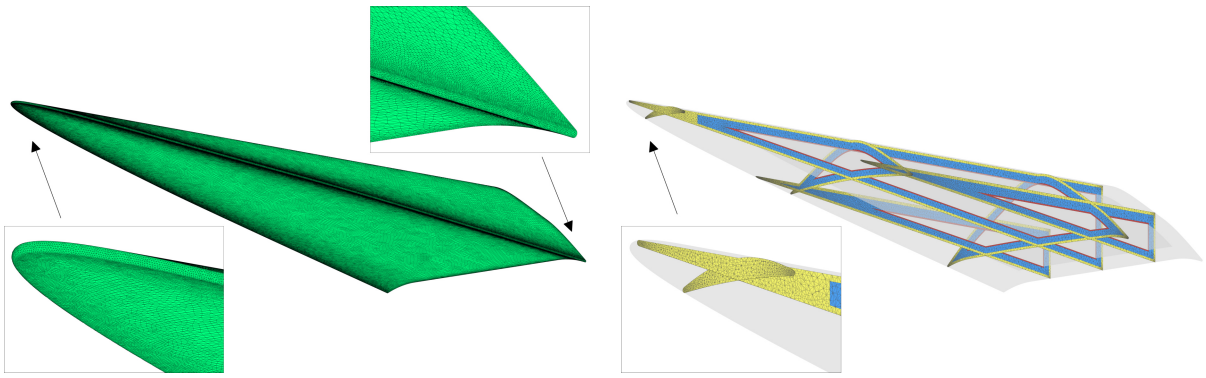

(a) CSM surface mesh. (b) CSM volume mesh cuts.

Fig 5. Power spectral densities of the wind profiles of the seven weather balloons.

Table 2. Used layers in structural model and their material.

Layer	**Thickness**	**Material**	**therm. Cond. Coeff.**	**Density**
Unit	[mm]		[W/(m K)]	[kg/m^3]
TPS	10	C/C-SiC	12.5 - 125.0	1900.0
Isolation	30	Zirkar ZO/ZYK	0.126 - 0.661	961.1
Inner Hull	5	Aluminum 7075	145.0	2800.0

this can be time consuming and computational expensive. Depending on the flight path this can easily lead to months of computation time. For this reason the design of an Aero-Thermal Databse (ATDB) [7] finds its application as the middle fidelity approach as a much faster surrogate model for heating.

The database consist of 11 selected time points at $\Delta t = 20\,\text{s}$ from the unsteady high fidelity solution by reusing their converged solution. Then a second steady solution at each point with a higher impinged surface temperature of $\Delta T = 200\,\text{K}$ is calculted. The selected points are shown in table 3 with their corresponding altitude, mach number and velocity.

This results in 2 data points at each given altitude to get a gradient to account for the influence of local wall temperature on the resulting heatflux.

This middle fidelity CFD solution by means of the new heatflux on the surface as a function of altitude and local surface temperature, get then interpolated on the CSM mesh along the unsteady solution process within $CoNF^2aS^2$. The CSM solver (Ansys 2022 R2) is the same, used for the high fidelity coupling scheme, lowering the computation time to some days for the whole $t = 450\,\text{s}$ trajectory. The calculated time steps are $\Delta t = 1.0\,\text{s}$.

4. Results

4.1. High fidelity / DLR TAU RF - Ansys

4.1.1. Differences between NEQ and EQ gas model

Figure 6 shows the general flow phenomena at the beginning of the unsteady coupled simulation at $t = 1.0\,\text{s}$ for the NEQ (figure 6(a)) as well as the applied EQ (figure 6(b)) model, described earlier.

In general they are comparable with some small differences in the temperature profile around the body, which then results in different heatflux solutions. First, the shock angle is slightly smaller for the NEQ solution with a lower temperature behind the shock. Second, the temperature distribution behind the base plate is much bigger for the EQ model, which results from the deflection around the base plane edge at the bottom of the HLRV.

Table 3. Chosen flight points for creation of database for bilinear heatflux interpolation.

Point	Time	Altitude	Mach Number	Velocity
Unit	[s]	[m]	[-]	[m/s]
1	0.0	85000.0	12.28	3364.3
2	20.0	78864.0	11.94	3374.7
3	40.0	70770.0	11.52	3388.3
4	60.0	60728.7	11.32	3405.0
5	80.0	48827.5	10.37	3421.7
6	100.0	35773.8	11.02	3417.5
7	120.0	25938.7	11.12	3325.0
8	140.0	24687.1	10.93	3260.5
9	160.0	26850.7	10.78	3231.1
10	180.0	29281.2	10.66	3212.6
11	200.0	31105.9	10.58	3199.4

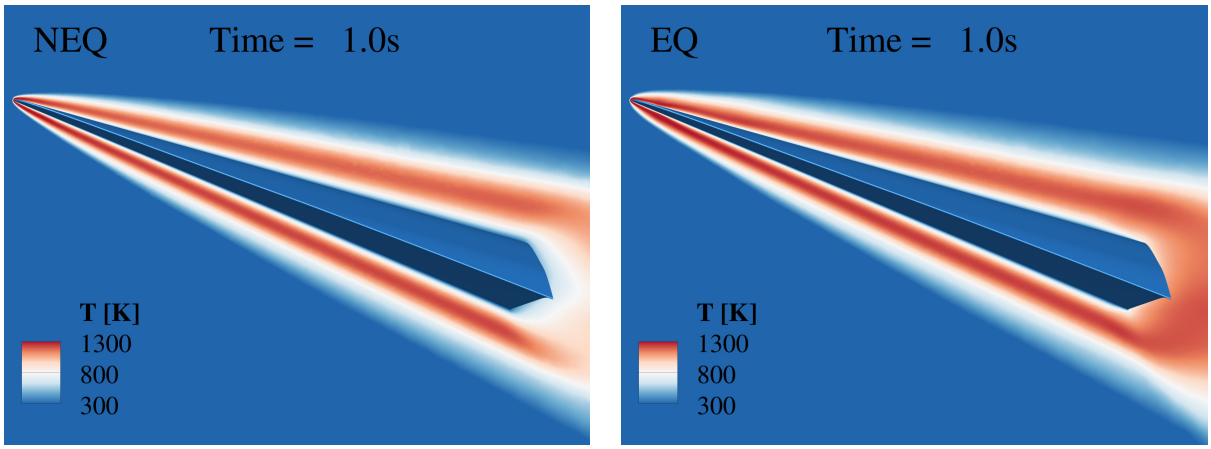

(a) NEQ. (b) EQ.

Fig 6. Differences in flow topology between NEQ and EQ at $t = 1.0\,\mathrm{s}$.

This can be seen in the temperature cut after $t = 50.0\,\mathrm{s}$ of flight time, presented in figure 7. Figure 7(a) shows 8 cuts in the body-fixed y-plane of the vehicle for both gas models. The peak differences of the higher computed NEQ model in the stagnation point reach $\Delta T = 5\,\mathrm{K}$ at $T = 782\,\mathrm{K}$. Along the leading edge the worst differences are under $6\,\mathrm{K}$, which is very near at each other.

At the bottom base plane edge the results start to differ by some margin. The peak temperature for the EQ model raises up to $\Delta T = 226\,\mathrm{K}$ higher, which results in a raised heating distribution to the end of the vehicle. The same can be seen in the temporal evolution of the leading edge point at the selected cuts shown in figure 7(b). The differences at the leading edge heating is small, but overshadowed by the huge discrepancies at the bottom base plate point depicted in *green* for NEQ and *blue* for the EQ model. As the NEQ gas model is the more sophisticated one these results are more trustworthy and therefore used for the following numerical results.

4.1.2. FSI coupled Trajectory from $0\,\mathrm{s} < t < 200\,\mathrm{s}$

Figure 8(a) shows the same cut and point positions for the simulated trajectory from 0 s to 200 s, using the NEQ gas model. After $\Delta t = 200\,\mathrm{s}$ the stagnation point reaches $2379\,\mathrm{K}$, which can be sustained by the C/C-SiC Material. The lines on top of each cut out show the heating of the luv side of the vehicle

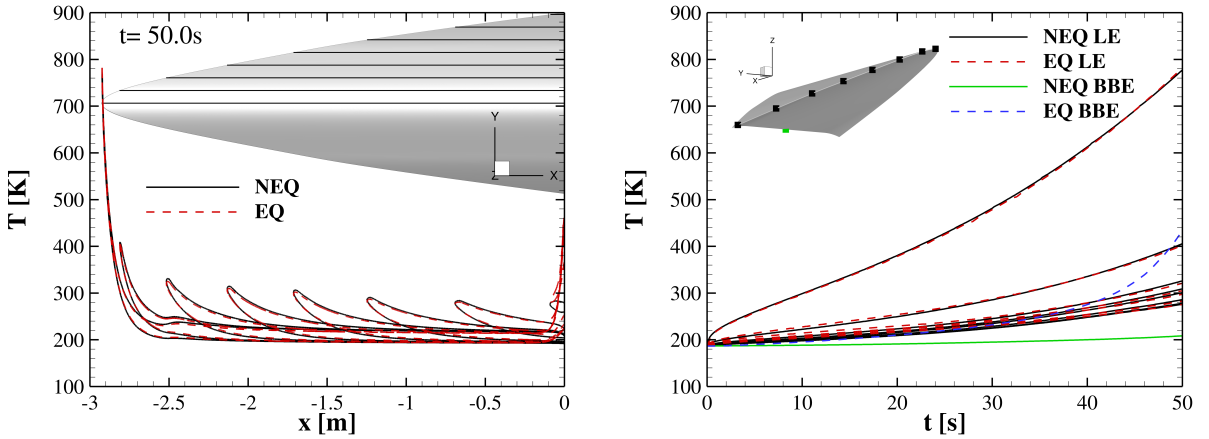

(a) Temperature distribution along x-direction in eight y-plane cuts from $0\,\text{m} < y < 0.56\,\text{m}$.

(b) Temperature evolution over time at leading edge and bottom base plane point.

Fig 7. Differences in structural heating between NEQ and EQ at $t = 50.0\,\text{s}$.

which is much higher due to the angle of attack during the reentry phase. The lines on the bottom are the lee side, which for most parts of the trajectory are not directly streamed against, hence the name lee side.

It is visible that the peak occurs very regional at the nose of the vehicle, as the leading edges almost reach the same temperature between $1631\,\text{K}$ and $1530\,\text{K}$ from $y > 0.16\,\text{m}$.

Figure 8(b) shows a peak at $t = 132\,\text{s}$ due to dipping into denser atmosphere. The nose tip heats up to $2749\,\text{K}$. Due to the transient heating through the body the time point where the peak heating occures changes along the leading edge, resulting at $1634\,\text{K}$ at $149\,\text{s}$ at the most spanwise y-cut at $y = 0.56\,\text{m}$. After the dipping point the altitude raises again, which leads to thinner atmosphere and falling temperature as the heating reduces almost converging towards a steady state heated through body radiating heat along the surface.

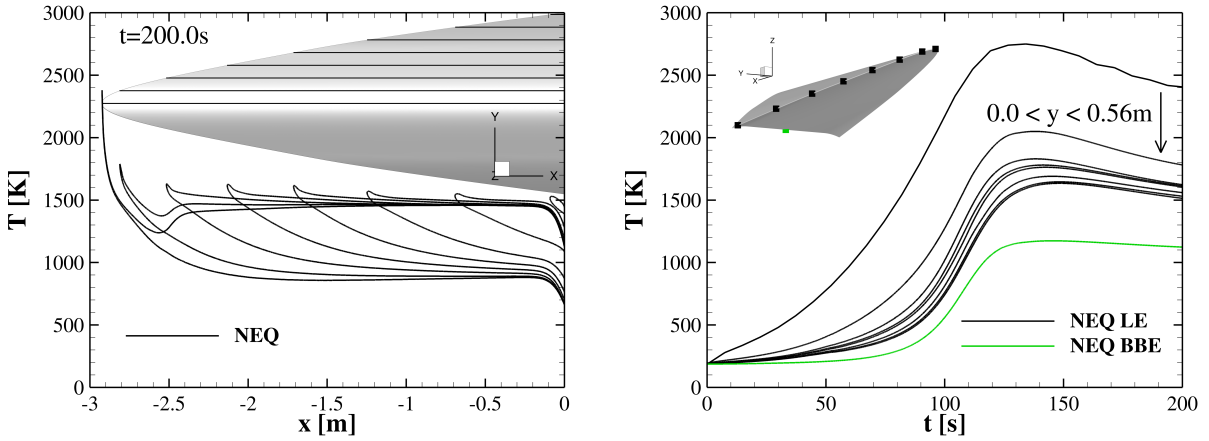

(a) Temperature distribution along x-direction in eight y-plane cuts from $0\,\text{m} < y < 0.56\,\text{m}$.

(b) Temperature evolution over time at leading edge and bottom base plane point.

Fig 8. High fidelity coupled FSI structural heating from $0\,\text{s} < t < 200.0\,\text{s}$.

4.1.3. Selected points for AeroThermal Database

Figure 9 illustrates six representative of the selected flight point which builds the heatflux database.

At the beginning of the calculation at $t = 0\,\text{s}$ the surface is cold, set by the atmospheric temperature according to ICAO at this height. In reality this is not accurate, as the vehicle has a history before this time point. Due to the lack of adequate solvers for higher altitudes like DSMC, this needs to be taken into account and will be discussed in the conclusion and outlook at the end of this work.

Along time, the temperature raises as is expected, leading to the smooth temperature distribution. The cold region behind the tip is due to the massive nose of the body, resulting in an heating reservoir to store energy in, which can be seen in the $y = 0\,\text{m}$ cut in figure 8(a) as well. The massive nose reduces the temperature on the luv side at around $x = -2.5\,\text{m}$ by about $\Delta T = 179\,\text{K}$ compared to the temperature at $x = -2.25\,\text{m}$.

Figure 9 displays the angle of attack of up to 12° during the reentry, followed by much smaller values during the glide phase of the spacecraft vehicle. To consider the angle of attack in the middle fidelity CFD solutions, two interpolation databases gets produced. The first combines the reentry points from 1 to 8 and the second database is build from flight points 8 till 11, adding point 5 at $h = 48.8\,\text{km}$ for the higher gliding altitude of the off design trajectory starting at $h = 85.0\,\text{km}$, which has to be in mind for the later consideration of results.

4.2. Mid fidelity / DLR TAU RF - ATDB heatflux interpolation

The mentioned bilinear interpolation as function of altitude and surface temperature inside the two databases are used as CFD solver within $CoNF^2aS^2$. The first database ranging from $85\,\text{km}$ until $24.7\,\text{km}$ and the second from $24.7\,\text{km}$ until $48.8\,\text{km}$. The switch between the databases is fixed at the dipping point of the trajectory at $t = 132\,\text{s}$.

4.2.1. FSI coupled Trajectory from $0\,\text{s} < t < 200\,\text{s}$

Figure 10 compares the mid fidelity solution with the fully coupled high fidelity results. Again the peak difference in temperature at the nose tip is $\Delta T < 8\,\text{K}$ by a total amount of $2387\,\text{K}$ in the interpolated case. In the worst case at $x = -2.0\,\text{m}$ of the symmetry cut the predicted temperatures are $\Delta T = 33\,\text{K}$ at $T = 1455\,\text{K}$ bigger at the luv side compared to the fully coupled solutions. Considering the much faster solution time these differences are negligible.

The heating on the lee side of the HLRV is matching very good between the two coupled procedure, because due to small surface heatfluxes it is dominated by the inbody heat conduction, which is calculated by the same CSM solver.

During the temperature evolution, shown in figure 10(b) over time, some oscillation between $t = 120\,\text{s}$ and $160\,\text{s}$ are present, where the interpolation databases lack the transition from reentry to glide phase. The biggest difference is $\Delta T = 108\,\text{K}$ at the leading edge at $t = 154\,\text{s}$, which again is reasonable. As the glide phase characteristics gets represented in great detail the much fast method can now be applied to calculate the trajectory in total from $0\,\text{s} < t < 450\,\text{s}$ in the following chapter.

4.2.2. FSI coupled Trajectory from $0\,\text{s} < t < 450\,\text{s}$

Along the whole considered trajectory, figure 11 presents the heating distribution at the end of the observed flight at $t = 450\,\text{s}$. The peak temperature falls to $T = 2485\,\text{K}$ at the nose tip. The rest of the vehicle heats throughout the body reaching between $1450\,\text{K} < T < 1550\,\text{K}$ at a luv side points of $0.15\,\text{m}$ away from the leading edge. The leading edge itself reaches values between $1838\,\text{K}$ and $1574\,\text{K}$ in all off symmetry cuts, which is reasonable to be handled by the choosen material mix in the structure.

The symmetry cut at $y = 0\,\text{m}$ shows a filled reservoir as the falling temperature dip vanishes inside the massive nose, which makes it heated through the entire body. The high tangential to surface in plane heat conduction coefficient of the TPS makes the heating distribution work as designed to cool the leading edge transporting heat inside the body to withstand the high loads during the dipping maneuver.

Figure 11(b) shows the converged temperature over time at the end of the trajectory analysis. The heating is in equilibrium with the radiation during the glide phase, which makes it radiation adiabatic.

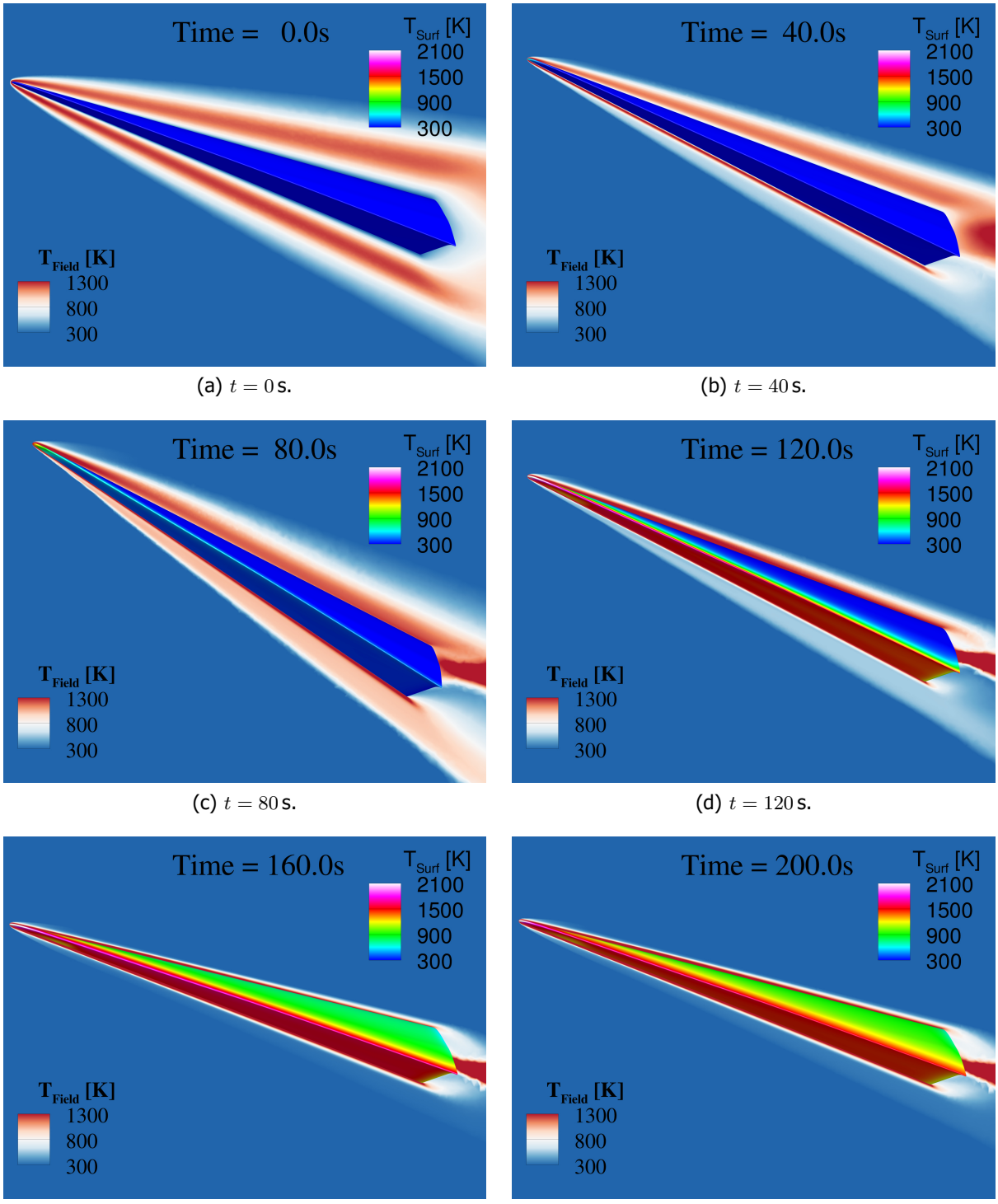

(a) $t = 0$ s. (b) $t = 40$ s.

(c) $t = 80$ s. (d) $t = 120$ s.

(e) $t = 160$ s. (f) $t = 200$ s.

Fig 9. Differences in flow topology between NEQ and EQ at $t = 1.0$ s.

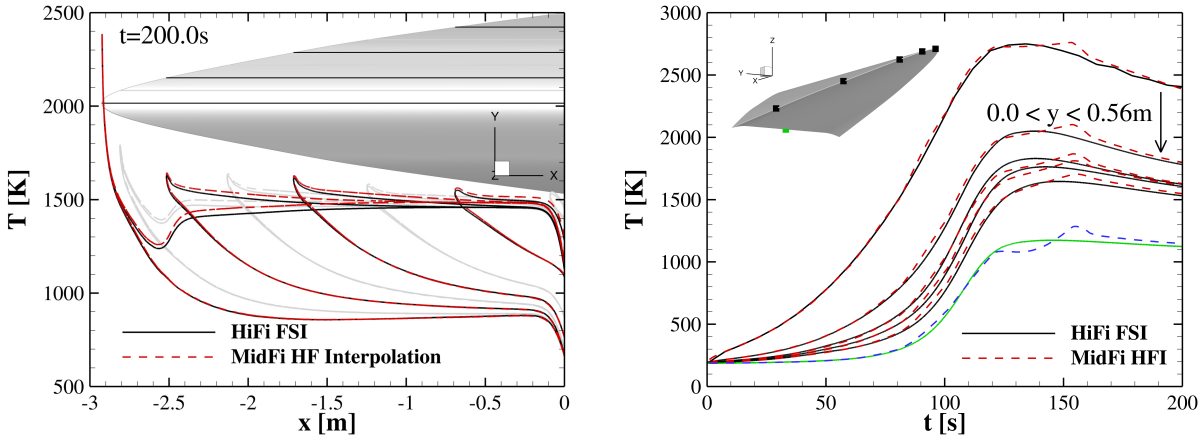

(a) Temperature distribution along x-direction in four y-plane cuts from $0\,\text{m} < y < 0.56\,\text{m}$.

(b) Temperature evolution over time at leading edge and base plane points.

Fig 10. Differences in structural heating between fully coupled FSI and heatflux interpolation from database at $t = 200.0\,\text{s}$.

This is an important information on its own, as this points to a geometry and trajectory combination, which has the thermal budget to actually fly. Considering the big safety factors, which the material can withstand this looks promising. The isolation for instance, can withstand continuously thermal conditions of up to $T = 2200\,\text{K}$ regarding to its datasheet.

4.2.3. FSI coupled off-design Trajectory from $0\,\text{s} < t < 450\,\text{s}$

This chapter uses the same interpolation databases for the designed trajectory starting at $h = 85\,\text{km}$, applying it to the shown off design flight path starting at $h = 75\,\text{km}$. Figure 12 shows the resulting temperature over time for the leading edge points in comparison to a newly created high fidelity coupled solution until $t < 73\,\text{s}$.

The heatflux interpolation routine overpredicts the nose tip temperature by $\Delta T = 30\,\text{K}$ at $T = 1437\,\text{K}$, which makes it the conservative approach. Along the leading edge points the differences get smaller

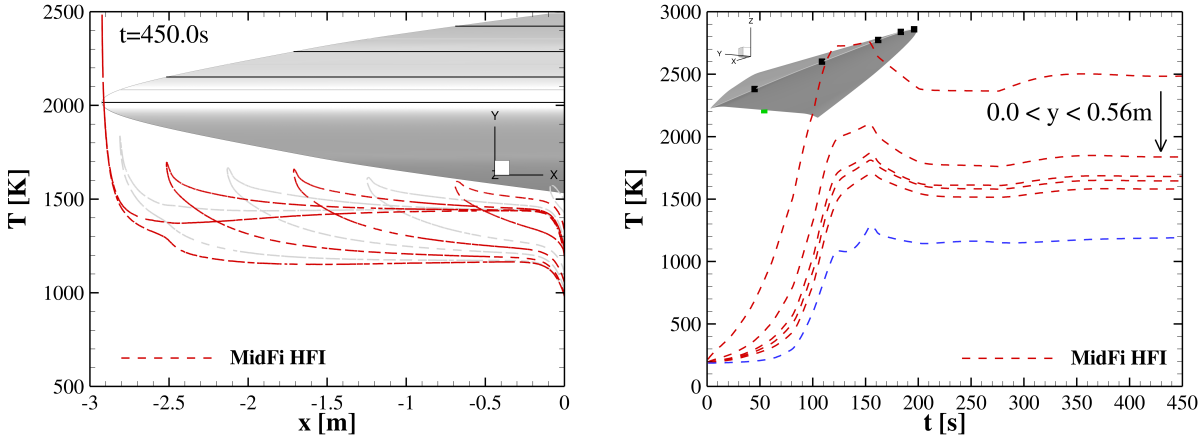

(a) Temperature distribution along x-direction in four y-plane cuts from $0\,\text{m} < y < 0.56\,\text{m}$.

(b) Temperature evolution over time at leading edge and base plane points.

Fig 11. Differences in structural heating between fully coupled FSI and heatflux interpolation from database at $t = 200.0\,\text{s}$.

down to $\Delta T = 9\,\text{K}$ at the y-cut at $0.56\,\text{m}$. Overall the agreement is very good.

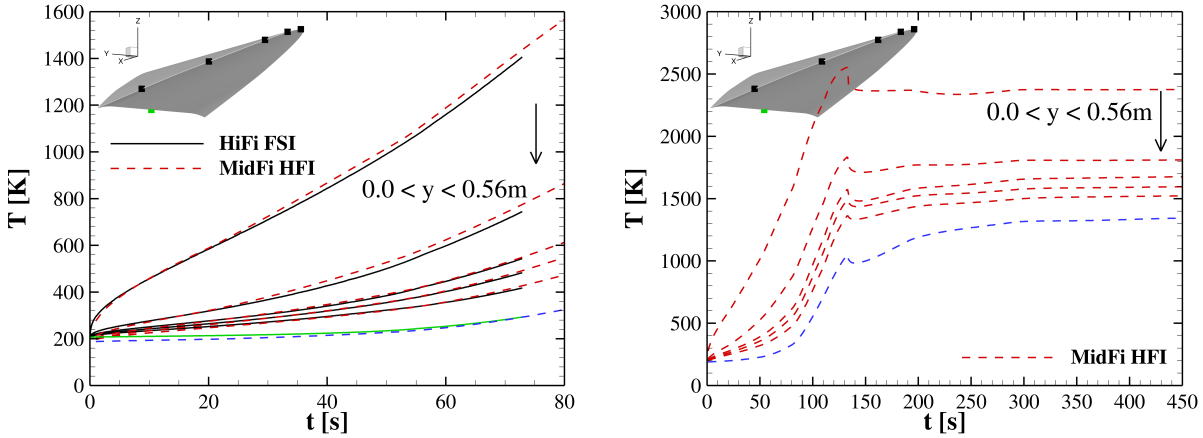

(a) Temperature distribution along x-direction in eight y-plane cuts from $0\,\text{m} < y < 0.56\,\text{m}$.

(b) Temperature evolution over time at leading edge and base plane points.

Fig 12. Differences in structural heating between fully coupled FSI and heatflux interpolation from database at $t = 200.0\,\text{s}$.

Figure 12(b) shows the temporal distribution of the selected point until the end of the considered off design trajectory. Again after $t > 200\,\text{s}$ a radiation adiabatic state of equilibrium is reached at leading edge temperatures between $2375\,\text{K}$ and $1522\,\text{K}$, which is about $\Delta T = 110\,\text{K}$ to $80\,\text{K}$ smaller compared to the initial trajectory. The main reason can be found in the $\Delta h = 5\,\text{km}$ higher altitude during the gliding phase of the HLRV, resulting in thinner atmospheric conditions and smaller heatfluxes on the surface. As the velocity is held the same between both trajectories the off-design case has a slighly smaller mach number of 9.8 compared to 10.0 at the end of the analyzed flight path.

The peaks in temperature at $t = 132\,\text{s}$ can be justified by the switch of the interpolation databases from the reentry DB to the gliding DB at this time point. As the equilibrium state is reached at the end of the simulation it is not expected to change the results much, if the database would have been adapted to the new flow conditions of the off design trajectory.

Afterall the results between the compared models show very good agreement, which make it possible to apply this kind of bilinear database interpolation for the heating of HLRVs, even if the trajectory changes during the design process, or depending on the structural sizing other glide altitudes needs to be targeted as shown.

5. Conclusion

This paper compares two different approaches in assessment of thermal loads of high lift reentry vehicles. First a designed generic vehicle and trajectory with starting point at $h = 85\,\text{km}$ gets calculated from $0\,\text{s} < t < 200\,\text{s}$ using a high fidelity unsteady coupled FSI approach with the DLR TAU code for CFD and Ansys for CSM solution. Using these numerical solutions at $\Delta t = 20\,\text{s}$, eleven time points where derived and a second solution is calculated with an added surface temperature of $\Delta T = 200\,\text{K}$ at each point. These flight points are then used to build two independent and faster responding surrogate aerothermal databases as a function of altitude and surface temperature for the reentry as well as the gliding phases.

The resulting heating evolution of the middle fidelity coupled approach only shows small differences and very good agreement compared with the higher fidelity results. Same can be said by analyzing the off design trajectory starting at $h = 75\,\text{km}$.

Considered the computational time and cost, the presented simpler method, can be used to calculate

the heating along the trajectory by over an order of magnitude faster resulting in marginal differences in calculated heating along the leading edge as well as inside the body.

From a design point of view the shown HLRV can withstand the faced aerothermal loads along both of the calculated trajectories. At each end a radiation adiabatic state of equilibrium is reached, meaning the thermal budget of the combination between geometry, trajectory and material mix is applicable at these flight conditions.

In the future, a multi-fidelity approach will be implemented and used to speed up the design process and still maintaining the accuracy of the high-fidelity methods by using ML and KI methods to select the specific methods along a trajectory. The goal is to use the faster methods along a broad design space and afterwards re-evaluating the error and reducing it with the more accurate but slower methods.

On a further node, the starting altitude and therefore resulting starting surface temperature at $t = 0\,\mathrm{s}$ will be elevated by the implementation of an DSMC method within the coupled process chain.

References

[1] Ansys Inc. Ansys. https://www.ansys.com/de-de/.

[2] Fynn Barz and Marius Franze. Comparison of Different Fidelity Approaches for the Coupled Aerothermodynamic Heating of Hypersonic Reentry Vehicle. In *HiSST: 3rd International Conference on High-Speed Vehicle Science Technology*, Busan, Korea, April 2024.

[3] Thino Eggers. *Aerodynamischer Entwurf von Wellenreiter - Konfigurationen für Hyperschallflugzeuge*. PhD thesis, Technische Universität Braunschweig, Deutschland, 1999.

[4] Sanford Gordon, Bonnie J. Mcbride, and Bonnie J. Mcbride. Computer program for calculation of complex chemical equilibrium compositions and applications. Part 1: Analysis. Report NASA-RP-1311, NASA Lewis Research Center, Cleveland, Ohio, USA, October 1994.

[5] Roop N. Gupta, Jerrold M. Yos, ichard A. Thompson, and Kam-Pui Lee. A Review of reaction Rates and Thermodynamic and transport Properties for an 11-Species Air Model for Chemical and Thermal Nonequilibrium Calculations to 30000K. Report NASA-RP-1232, NASA, 1990.

[6] Stefan Langer, Axel Schwöppe, and Norbert Kroll. The DLR Flow Solver TAU - Status and Recent Algorithmic Developments. In *52nd Aerospace Sciences Meeting*, National Harbor, Maryland, January 2014. American Institute of Aeronautics and Astronautics.

[7] Mariasole Laureti and Sebastian Karl. Aerothermal databases and load predictions for Retro Propulsion-Assisted Launch Vehicles (RETALT). *CEAS Space Journal*, 14(3):501–515, July 2022.

[8] Mariasole Laureti and Sebastian Karl. Aerothermal Analysis of the RETALT2 SSTO Vehicle. In *10th EUCASS - 9th CEAS - 9th CEAS 2023*, Lausanne, Switzerland, July 2023.

[9] A. Mack and Volker Hannemann. Validation of the Unstructured DLR-TAU-Code for Hypersonic Flows. In *32nd AIAA Fluid Dynamics Conference and Exhibit, AIAA Paper 2002-3111*, pages 1–9, St. Lousi, Missouri, 2002.

[10] Michael Meinel and Gunnar ´Olafur Einarsson. The FlowSimulator framework for massively parallel CFD applications. In *State of the Art in Scientific and Parallel Computing*, University of Iceland, Reykjavi, June 2010.

[11] NOAA, NASA, and U.S. Air Force. U.S. Standard Atmopshere 1976. Report NASA-TM-X74335, Washington D.C., USA, 1976.

[12] Lars Reimer, Ralf Heinrich, Sven Geisbauer, Tobias Leicht, Stefan Görtz, Markus Raimund Ritter, and Andreas Krumbein. Virtual Aircraft Technology Integration Platform: Ingredients for Multidisciplinary Simulation and Virtual Flight Testing. In *AIAA Scitech 2021 Forum*, Virtual Event, January 2021.

[13] Andreas Schütte. *Wirbelumströmungen an gepfeilten Flügeln mit runden Vorderkanten*. DLR Forschungsbericht 2015-40, Dissertation, Technische Universität Braunschweig, Deutschland, 2015.

[14] Dieter Schwamborn, Thomas Gerhold, and Ralf Heinrich. The DLR TAU-Code: Recent Applications in Research and Industry. *European Conference on Computational Fluid Dynamics, ECCOMAS CFD*, pages 1–25, 2006.

[15] Philippe R. Spalart and Steven R. Allmaras. A One-Equatlon Turbulence Model for Aerodynamic Flows. In *30th Aerospace Sciences Meeting & Exhibit*, Reno, Nevada, USA, 1992.

[16] Yasuh Wada and Meng-Sing Liou. An Accurate and Robust Flux Splitting Scheme for Shock and Contact Discontinuities. 18(3):633–657, 1997.